



OPEN ACCESS

EDITED BY

Xiaohui Xie,
Ministry of Natural Resources, China

REVIEWED BY

Zhumin Lu,
South China Sea Institute of Oceanology
(CAS), China
Haijin Cao,
Hohai University, China

*CORRESPONDENCE

Fei Yu
[✉ yuf@qdio.ac.cn](mailto:yuf@qdio.ac.cn)

SPECIALTY SECTION

This article was submitted to
Physical Oceanography,
a section of the journal
Frontiers in Marine Science

RECEIVED 06 December 2022

ACCEPTED 10 March 2023

PUBLISHED 24 March 2023

CITATION

Zheng T, Yu F, Ren Q, Nan F,
Chen Z, Liu F, Hu Y and Ding Y-n (2023)
Near-inertial waves generated by typhoon
MITAG under the influence of anticyclonic
eddy east of Taiwan.
Front. Mar. Sci. 10:1117197.
doi: 10.3389/fmars.2023.1117197

COPYRIGHT

© 2023 Zheng, Yu, Ren, Nan, Chen, Liu, Hu
and Ding. This is an open-access article
distributed under the terms of the [Creative Commons Attribution License \(CC BY\)](https://creativecommons.org/licenses/by/4.0/). The
use, distribution or reproduction in other
forums is permitted, provided the original
author(s) and the copyright owner(s) are
credited and that the original publication in
this journal is cited, in accordance with
accepted academic practice. No use,
distribution or reproduction is permitted
which does not comply with these terms.

Near-inertial waves generated by typhoon MITAG under the influence of anticyclonic eddy east of Taiwan

Tongtong Zheng^{1,2,3}, Fei Yu^{1,2,3,4,5*}, Qiang Ren^{1,3,4}, Feng Nan^{1,3,4,5},
Zifei Chen^{1,3}, Yansong Liu^{1,3,4}, Yibo Hu^{1,2,3} and Ya-nan Ding⁶

¹Institute of Oceanology, Chinese Academy of Sciences, Qingdao, China, ²College of Marine Sciences, University of Chinese Academy of Sciences, Beijing, China, ³CAS Key Laboratory of Ocean Circulation and Waves, Chinese Academy of Sciences, Qingdao, China, ⁴Center for Ocean Mega-Science, Chinese Academy of Sciences, Qingdao, China, ⁵Marine Dynamic Process and Climate Function Laboratory, Pilot National Laboratory for Marine Science and Technology (Qingdao), Qingdao, China, ⁶Key Laboratory of Marine Environmental Information Technology, National Marine Data and Information Service, Ministry of Natural Resources, Tianjin, China

Based on subsurface mooring observations and HYCOM data, a complete investigation was conducted of the near-inertial waves (NIWs) caused by Typhoon MITAG to the east of Taiwan. HYCOM data were mainly used to reveal the role played by anticyclonic eddies in the propagation of NIWs. The results show that most typhoon-generated NIWs propagate towards negative vorticity, and NIWs near the edge gradually accumulated towards the eddy center and down to 800 m. NIWs propagating through the thermocline to the deep ocean were mainly concentrated in the eddy, and the near-inertial energy flux showed a significant enhancement from 400 to 600 m. Moreover, the downwards propagation of NIWs in the eddy enhanced the kinetic energy of background flow. NIWs outside the anticyclonic eddy dissipated quickly, while inside the eddy, there were high value areas of e-folding time. Dynamic mode decomposition illustrates that the anticyclonic eddy mainly captures higher modes of NIWs, and the state of continuous energy growth of higher modes can be maintained for more than a week. In addition, NIWs can also be carried westwards by the advection of the mean background flow at the eddy's edge.

KEYWORDS

near-inertial waves, typhoon, HYCOM data, anticyclonic eddy, energy flux, background flow

1 Introduction

Near-inertial waves (NIWs) with a frequency near the inertial frequency f appear as prominent peaks in both the continuum internal wave spectrum and the shear spectrum (Alford and Whitmont, 2007; Silverthorne and Toole, 2009). They are an important constituent of high-frequency oscillations in the ocean (Alford et al., 2016) and are widespread globally

(Webster, 1968). There is significant variability in both the spatial and temporal distributions of NIWs (Liu et al., 2019), such as seasonality (Chen et al., 2013; Whalen et al., 2018) and differences between latitudinal bands (Elipot et al., 2010; Alford, 2020). NIWs are not only important carriers for the transmission of wind energy to the deep ocean (Greatbatch, 1984; Price et al., 1986) but also one of the main energy sources for deep ocean internal waves (Alford, 2003; Furuichi et al., 2008; Flexas et al., 2019). Therefore, NIWs play a crucial role in air-sea fluxes, ocean mixing and energy dissipation and have a nonnegligible impact on climate (Jochum et al., 2013).

Unsteady wind fields are an important source of NIWs (Alford et al., 2012), in which tropical cyclones (TCs) are the most typical processes due to relatively intense and transient wind stress. TCs can instantaneously generate strong near-inertial kinetic energy (NIKE) in the mixed layer along their path. Most of the NIKE is transmitted into the thermocline and deeper layers by NIWs (D'Asaro et al., 1995; Alford, 2001; Jiang et al., 2005), with some of them even reaching layers deeper than 1000 m [30], demonstrating their potential importance in mixing the deep ocean. Previous studies suggest that typhoon-generated NIWs have horizontal wavelengths of hundreds to thousands km in the upper ocean (Hisaki and Naruke, 2003; Johnston et al., 2021) and large vertical group velocities (tens to hundreds m per day) (Sun L. et al., 2011; Sun Z. et al., 2011; Yang et al., 2015; Hou et al., 2019; Yu et al., 2022). The frequency of these NIWs experiences a redshift (frequency below the local inertial frequency f) or a blueshift (frequency above f) under different background flows (Sun L. et al., 2011; Sun Z. et al., 2011; Chen et al., 2013; Pallas-Sanz et al., 2016; Hou et al., 2019). There is now a relatively adequate characterization of typhoon-induced NIWs. However, the difficulty of obtaining three-dimensional *in-situ* observations limits our understanding to some extent. Exploration of typhoon-induced NIWs using reliable model data is needed.

The propagation of NIWs in the ocean interior occurs with different modes, with almost all depth-integrated near-inertial horizontal energy fluxes projected onto the first five modes (Raja et al., 2022). Different modes can reflect the vertical structure of internal waves (Greatbatch, 1984). It is generally accepted that low-mode internal waves are more stable and high-mode waves are dissipative (Nikurashin and Legg, 2011; Simmons and Alford, 2012). However, the mode structure of NIWs has been less explored than that of internal tides and internal solitary waves. Some observations suggest that the vertical structure of typhoon-generated NIWs is dominated by the second baroclinic mode, while the first mode is not significant due to its large horizontal scale (Chen et al., 2013). Studies using HYCOM data demonstrate that NIWs with small e-folding time are dominated by the first three modes, while those with larger e-folding time are gradually controlled by higher modes, which may be related to the interaction of NIWs and mesoscale eddies (Cao et al., 2021). These previous studies illustrate that the investigation of mode structure is important for understanding both the propagation and energy dissipation of NIWs.

Under the influence of the beta-dispersion effect, the horizontal scale of wind-generated near-inertial motion in the mixed layer will decrease, thereby increasing the propagation speed of NIWs and allowing the near-inertial energy to propagate farther away (Gill, 1984). The vorticity of mesoscale eddies that are inhomogeneously spatially distributed has the same effect on NIWs. Mesoscale eddies can also influence the way winds input energy to the ocean by shifting the resonant frequency from local f to effective Coriolis frequency f_{eff} (WELLER, 1982; Kunze, 1985). A global model shows that divergence of NIKE and near-inertial energy flux are strongly modulated by the background vorticity, with most of the horizontal energy flux converging in anticyclonic eddies (Raja et al., 2022). Many observations have confirmed that anticyclonic eddies are more conducive to the enhancement and propagation of NIWs to the deep ocean (Lee and Niiler, 1998; Park and Watts, 2005; Jaimes and Shay, 2010), whereas cyclonic eddies confine NIWs to the mixed layer and allow them to propagate out of eddies (Zhang et al., 2018). In the region of negative vorticity, wind-generated NIWs are not able to escape freely. These NIWs are then trapped and stay in the critical layer of anticyclonic eddies. These NIWs, which continue to accumulate in the critical layer, can release energy through transfer to the mean flow, turbulent mixing and dissipation or wave-wave interactions (Kunze, 1985). At present, studies related to the release of near-inertial energy in mesoscale eddies are rare. In addition, horizontal flow shear can also influence NIWs by modulating f_{eff} . There was a significant elevation of NIKE in the Kuroshio. The negative vorticity region of the Kuroshio acts as a waveguide, advecting NIWs to the northeast over 300 km (Rainville and Pinkel, 2004; Jeon et al., 2019).

The subtropical northwest Pacific has complex multiscale oceanic dynamic processes (Hu et al., 2015) and is also characterized by an abundance of TCs (Hu et al., 2020). Due to the difficulty of implementing marine observations, most previous studies have focused on the South China Sea (Huang et al., 2021; Yang et al., 2021), and research on NIWs east of Taiwan, where mesoscale processes are highly active, remains limited. In this paper, by comparing observations with HYCOM data, we confirmed that HYCOM data can effectively simulate the typhoon-generated NIWs east of Taiwan during Typhoon MITAG. Therefore, the HYCOM data was used to explore the reasons for the differences between mooring observations of the same near-inertial event and the influence of mesoscale eddies on the propagation of NIWs.

This paper is organized as follows. The moorings, typhoon information and HYCOM data together with methodology are introduced in Section 2. The *in-situ* observations and HYCOM data are compared in Section 3. In Section 4, the generation and propagation of NIKE generated by Typhoon MITAG are discussed, focusing on e-folding time, near-inertial energy flux inside and outside an anticyclonic eddy and the release of near-inertial energy. In Section 5, the mode composition is performed and a case analysis along the zonal section where the moorings are located is provided. Finally, the main conclusions are summarized in Section 6.

2 Data and methods

2.1 Mooring observations

Two subsurface moorings were deployed in the Northwest Pacific east of Taiwan from August 2019 to December 2020 (Figure 1), and each mooring was equipped with two 75 kHz Teledyne RDI acoustic Doppler current profilers (ADCPs). The details of the mooring deployments are listed in Table 1. After pre-processing (including depth correction, quality control, etc.), the velocity data are interpolated onto standard layers with intervals of 5 m. Depending on the depth of propagation of the near-inertial events of interest in this paper, data from 50 to 800 m were used primarily for the follow-up study.

2.2 Typhoon MITAG

Typhoon MITAG formed as a tropical depression near 13.0°N, 138.9°E in the morning of 27 September 2019 and then moved northwest with a maximum wind speed of ~13 m/s. Then, MITAG entered the sea area east of Taiwan at 08:00 on 30 September while changing its direction to the north, and strong winds (wind speed exceeding 15 m/s) began to affect the observation points. On 30 September, MITAG passed between the two moorings, and the path of the typhoon center was closer to C06 (Figure 1). After passing the moorings, MITAG made landfall in mainland China on 1 October. The typhoon best track data were downloaded from The Regional Specialized Meteorological Center (RSMC) Tokyo-Typhoon center

(http://www.jma.go.jp/jma/jma-eng/jmacenter/rsmc-hp-pub-eg/RSMC_HP.htm).

2.3 Near-inertial kinetic energy calculations

A Butterworth bandpass filter was applied to obtain the near-inertial horizontal velocity (u, v). The frequency band of $0.9-1.12f$ (f is the local Coriolis parameter) was selected according to the results of power spectrum analysis (Figure S1). Then, NIKE was calculated as:

$$NIKE = \rho_0(u^2 + v^2)/2 \tag{1}$$

where ρ_0 is the average density of seawater ($1.025 \times 10^3 \text{ kg/m}^3$). Estimates of background flow are derived by applying a low-pass filter of 10 days to the original velocity records to remove the influences of tides and mesoscale eddies.

2.4 Satellite altimeter data

The altimeter product used in this paper is the sea level anomaly (SLA) and geostrophic velocity anomaly data provided by Ssalto/Duacs, which is distributed in real time through the Copernicus Marine and Environment Monitoring Service (CMEMS). These data are utilized to resolve the range of anticyclonic eddies and to calculate sea surface vorticity. The dataset has a spatial resolution of $0.25^\circ \times 0.25^\circ$ and a temporal resolution of 1 d and is widely used in NIWs and mesoscale eddy-related studies.

2.5 Slab model

To calculate the wind energy flux input to the mixed layer during the transit of MITAG, the slab model (Pollard and Millard, 1970) and 10 m wind were adopted in this study. The wind data were derived from the European center for Medium-Range Weather Forecasts (ECMWF) global reanalysis ERA5 product, and its temporal and spatial resolutions are 1 h and $0.25^\circ \times 0.25^\circ$ (<https://cds.climate.copernicus.eu/cdsapp#!/dataset/reanalysis-era5-single-levels?tab=form>). The 10 m wind was first converted into wind stress. Then, the corresponding flow velocity in the mixed layer can be calculated as follows:

$$\begin{cases} \frac{dZ}{dt} + (r + if)Z = \frac{\tau}{H} \\ Z = u + iv \\ \tau = \tau_x + i\tau_y \end{cases} \tag{2}$$

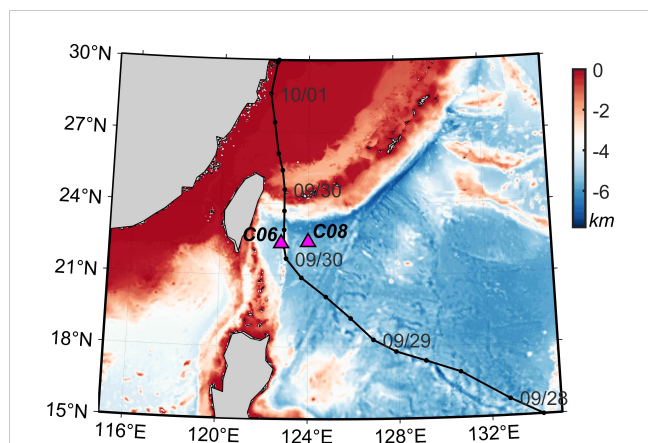


FIGURE 1 Topography east of Taiwan and trajectory of Typhoon MITAG (black line and dots). Pink triangles represent the locations of the ADCP moorings. Time corresponding to some of the black dots is marked in gray letters.

TABLE 1 Mooring deployment details.

Name	Location	Sampling interval	Bin size	Range Depth
C06	122.77°E; 22.34°N	1 h	8 m	50-800 m
C08	123.99°E; 22.40°N	1 h	8 m	50-800 m

where Z are the velocities of the meridional and zonal flows in the mixed layer, τ is wind stress, f is the local Coriolis parameter, H is the mixed layer depth and r is the damping coefficient of inertial motions. The flow in the mixed layer can be expressed as the sum of the Ekman component and the near-inertial component. Alford (Alford, 2003) refined the model by applying a Fourier transform to the wind stress, resulting in the solution of Equation (2) as:

$$R(\sigma) = \frac{1}{H} \frac{r - i(f + \sigma)}{r^2 + (f + \sigma)^2} \quad (3)$$

The Ekman component is:

$$R_E(\sigma) = \frac{1}{H} \frac{r - if}{r^2 + f^2} \quad (4)$$

Then, the inertial component is $R_I = R + R_E$, and finally, the wind-generated near-inertial energy flux is obtained by inversion of the Fourier transform.

2.6 Dynamic mode decomposition

NIWs can be represented by the superposition of multiple discrete baroclinic modes in the ocean interior (Gill, 1982; D'Asaro et al., 1995). The vertical structure of each mode is governed by (Gill, 1982; Thorpe and Jiang, 1998):

$$\begin{cases} \frac{\partial^2 \Phi_n(z)}{\partial z^2} + \frac{N^2(z)}{c_n^2} \Phi_n(z) = 0 \\ \Phi_n(0) = 0; \Phi_n(-H) = 0 \end{cases} \quad (5)$$

where n is the mode number, c_n is the separation constant (eigenvalue), H is the water depth, and Φ_n denotes the eigenfunction and represents the baroclinic mode structure of vertical undulations and vertical flow. The buoyancy frequency N can be expressed as follows:

$$N^2(z) = -\frac{g}{\rho_0} \frac{\partial \rho(z)}{\partial z} \quad (6)$$

where g is the acceleration of gravity. The baroclinic mode structure of the horizontal flow can be obtained according to two equations:

$$\Pi_n = \rho_0 c_n^2 \frac{d\Phi_n(z)}{dz} \quad (7)$$

$$\Phi_n(z) = -\frac{1}{N^2(z)\rho_0} \frac{d\Pi_n}{dz} \quad (8)$$

Thus, the baroclinic flow for each mode can be expressed in terms of the vertical structure and time variation:

$$u(z, t) = \sum_{n=0}^N u_n(t) \Phi_n(z) \quad (9)$$

where $u(z, t)$ is the near-inertial velocity and $u_n(t)$ is the velocity of mode n . In this paper, mode decomposition of near-inertial velocities from moorings and Hybrid Coordinate Ocean Model

(HYCOM) data was carried out separately to investigate the dynamic structure. The version of the HYCOM data was GLBy0.08 with a temporal resolution of 3 h and a spatial resolution of $0.08^\circ \text{ lon} \times 0.04^\circ \text{ lat}$ and was divided vertically into 40 layers, which clearly reveal the energy propagation characteristics of NIWs (<https://www.hycom.org/dataserver/gofs-3pt1/analysis>). Considering the lack of temperature and salinity observations at the mooring sites and to facilitate calculations, the averages of HYCOM temperature and salinity during the duration of NIWs generated by MITAG were used to compute $N^2(z)$.

3 Comparisons between observations and HYCOM data

Observations showed that NIWs generated by Typhoon MITAG have vastly different characteristics at two moorings that are very close to each other (Figure 2B). The NIKE recorded by C06 is active above 200 m and is discontinuous with the deeper weaker NIKE, without obvious direct downwards propagation. The NIKE observed at C08 is characterized by rapid downwards propagation, with strong energy reaching 800 m within a week. Moreover, after the passage of MITAG, the vorticity at C06 was positive and became negative after October 8, while the vorticity at C08 remained negative (Figure 2A). SLA shows that an anticyclonic eddy affects C08 but not C06 (Figure S2). Considering the lack of three-dimensional observation data, the next expectation is to explore the reasons for the differences in NIKE at the two moorings, propagation characteristics of this near-inertial event and the effect of anticyclonic eddies on NIWs with HYCOM data.

Figure 2 also displays the near-inertial zonal currents and NIKE of the observations and HYCOM. NIWs extracted from HYCOM show good agreement with those from observations: they both propagate downwards to a shallower depth at C06 and have a clear discontinuity with the deep NIKE after mid-October, while at C08, they contain more energy and spread rapidly downwards to 800 m. This result preliminarily verifies the accuracy of the HYCOM data. It should be noted that the zonal currents and NIKE of HYCOM were smaller than observations at C06 and C08. The duration of HYCOM above 200 m is shorter at C06. Nevertheless, these differences may only have a limited influence on the propagation of NIWs in and outside the mesoscale eddies which is the main focus of this study.

The dynamic mode decomposition of near-inertial currents for both observations and HYCOM is shown in Figure 3. The first 20 modes are sufficient to simulate the original near-inertial velocity. For observations, at C06, the energy contained in the first three modes is similar just after the passage of MITAG, followed by a gradual strengthening of the first and second modes, reaching peaks in mid-October and then decaying. At C08, the first three modes strengthens and then decays rapidly, with the first two modes accounting for the major contribution. At the beginning of the typhoon's transit which is 30 September, the first, second and third modes at C06 accounted for 14.60%, 11.10% and 12.82%

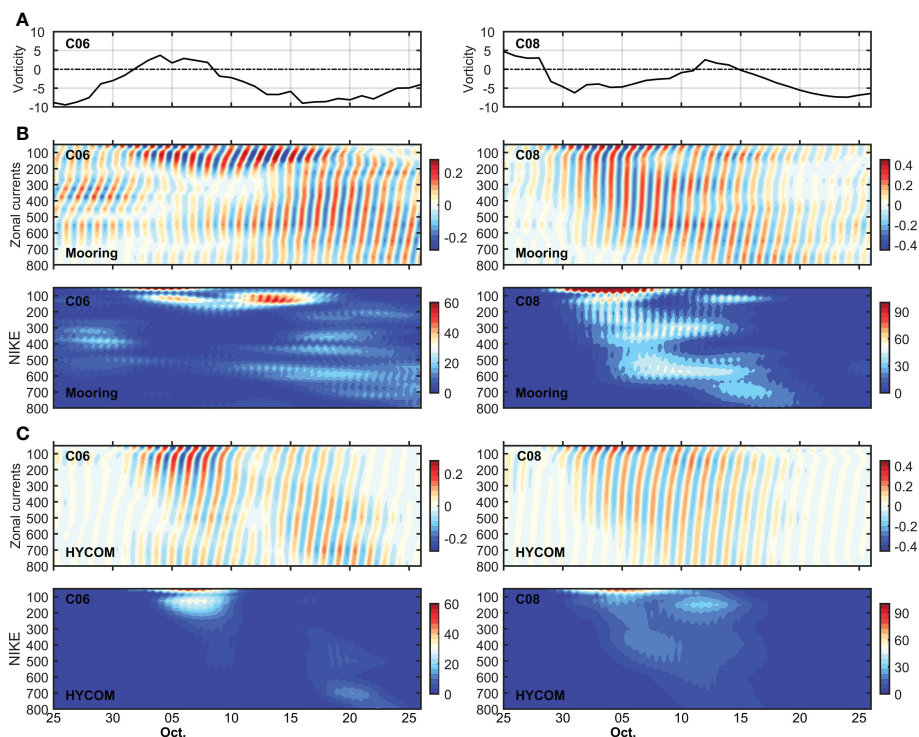


FIGURE 2 Variation of the sea surface vorticity (A), (unit: $10^{-6}/s$). Zonal currents (unit: m/s) and NIKE (unit: J/m^3) of mooring observations (B) and HYCOM (C) generated by MITAG at C06 and C08.

respectively. It indicates that typhoon-generated NIWs are dominated by the first mode at the beginning of generation, which agrees with Shay (Shay et al., 1989).

The HYCOM data is basically able to simulate the two peaks and long duration of different modes at C06 and the dominance and rapid dissolution of the second mode at C08. The downside is that the first mode of HYCOM contains less energy, and there is a gap between the total NIKE of observations and HYCOM (the

observations are higher). This is reasonable because HYCOM cannot fully include all complex ocean processes, such as tides. Though the third mode of HYCOM (Table 2) shows a high energy bias, the percentages of different modes for observations and HYCOM data are very similar over the entire near-inertial event. They both have the largest proportion of the second mode, followed by the first and third modes. At C08, the sum of the first three modes accounts for 80%, while at C06, they account for only 50%,

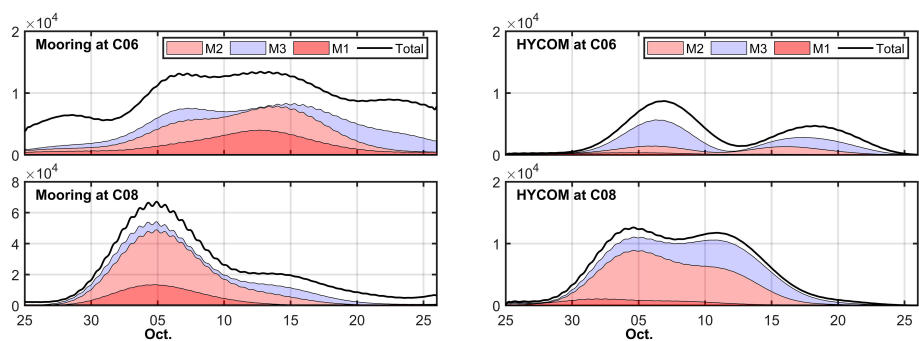


FIGURE 3 Time evolution of depth-integrated kinetic energy of different modes (unit: J/m^2), where M1, M2, M3 and Total denote the first, second and third mode and total NIKE respectively.

TABLE 2 Percentage of different modes.

Data		Mode1	Mode2	Mode3	Σ Mode1-3
C06	Mooring	14.5	19.4	14.8	48.8
	HYCOM	4.7	16.3	38.6	59.6
C08	Mooring	15.7	43.4	13.9	73.0
	HYCOM	7.1	50.2	30	87.3

showing a huge difference in the vertical structure of the NIWs. Therefore, the results of the dynamic mode decomposition of HYCOM data are reliable.

4 The generation and propagation of NIKE

4.1 Roles of wind

First, the input of wind energy is explored. The near-inertial energy flux in the mixed layer calculated from the slab model is shown in Figure 4. Before and after the passage of MITAG, the wind field east of Taiwan was relatively stable, bringing no significant near-inertial energy flux. Between 6:00 and 18:00 on 29 September, the near-inertial energy flux was mainly caused by winds from the northwest of the typhoon center. Then, MITAG fed a large amount

of near-inertial energy into the Kuroshio on the west side of its path and into the area near mooring C08 on the east side. After 6:00 pm on 30 September, MITAG gradually weakened along with the reduction in energy flux and then left the sea area east of Taiwan. As the main source of this near-inertial event, MITAG generates a strong energy flux mainly in the region west of 126°E, which corresponds well with the spatial distribution of NIKE in Section 4.2.

Mooring C06 is located on the path of the typhoon center, while C08 is on the right side. In the Northern Hemisphere, the wind stress above the mooring on the right side of the TC's path was deflected clockwise due to the movement of the TC, leading to strong NIWs (Kim et al., 2013; Chen et al., 2015). The results of the slab model illustrate that there was more energy input to the near-inertial band at C08 with a flux maximum of 0.98 W/m² compared to 0.47 W/m² at C06. This could explain the difference in the amount of NIKE contained in the upper layer at the two moorings.

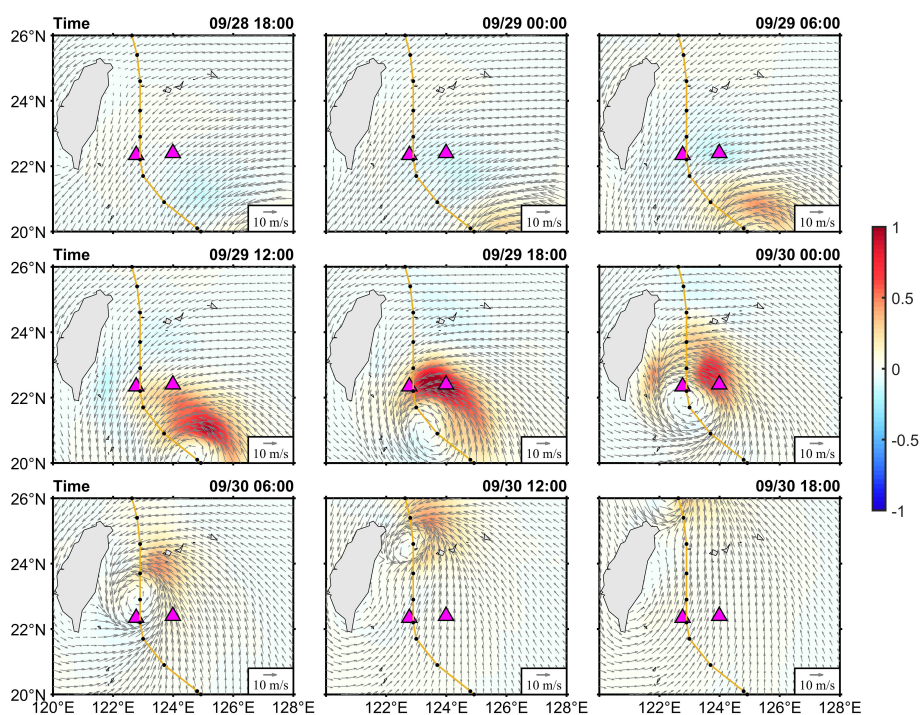


FIGURE 4 The near-inertial energy flux in the mixed layer (color shading, unit: W/m²) calculated from slab model and wind speed (arrows) from 26 to 30 September 2019. The yellow lines represent the trajectory of Typhoon MITAG.

However, sea surface winds cannot directly affect the propagation of NIWs in the ocean interior, and it was not the fundamental cause of the disparity in propagation.

4.2 Temporal and spatial variations

The near-inertial flow was extracted by bandpass filtering of the original HYCOM velocity data, and then the time evolution of NIKE at different depths was obtained, as shown in Figures 5, 6. The 50/100/200 m, 400 m and 800 m were chosen to represent the distribution of NIKE in the upper, middle and deep layers, respectively. Additionally, the edge of the anticyclonic eddy was represented by the closed SLA contour of the outermost circle of the eddy center (Chelton et al., 2011). Before the arrival of MITAG (Figure 5, 26 September), NIKE east of Taiwan was very weak, existing only at the south edge of the eddy. As MITAG approached, powerful NIKE was quickly excited along the typhoon's path in the upper layer. NIKE reached the maximum value and was most widespread at 50 m on 4 October. At this time, the NIWs had propagated to 400 m. Then, NIKE at 50 m faded away due to dissipation and downwards propagation. NIKE at 100 m and 200 m split into two parts: one at the west edge of the eddy and limited within the eddy, and the other rapidly dissipating near mooring C06, which completely disappeared by 12 October (Figure 6).

Influenced by anticyclone eddies, NIWs may be horizontally trapped and thus confined in the eddy, or may propagate outwards after encountering seawater with a higher f_{eff} than the intrinsic frequency (Kunze, 1985). As NIWs enter the anticyclone eddy, a portion of the energy is reflected and then propagates westward. Therefore, NIKE at 400 m gradually accumulated and intensified on the west edge of the eddy before October 9. The other part of the energy is captured and propagated downward, but remains biased towards the west periphery of the eddy at 400 m and 800 m. This is related to the location of the near-inertial energy source and the vertical structure of the anticyclone eddy. The vertical structure of the eddy may be asymmetric, with the center gradually shifting westwards with increasing depth, like a lens-shaped eddy (Lin et al., 2015). In the deep layer, NIKE was only enhanced two weeks after the passage of MITAG and initially only occurred inside the eddy. The NIKE at 800 m was not fully dissipated until 24 October. This near-inertial event lasted for more than 3 weeks.

These results suggest that Typhoon MITAG can rapidly generate widespread NIWs near its path in the upper layer and that these NIWs tend to propagate downwards and accumulate in areas of negative vorticity. The time taken for NIWs to propagate to 200 m was approximately 3 days and to 400 m was 6 days. Under the mixed layer, the NIWs outside the anticyclonic eddy did not cross the thermocline and dissipated within a week, while NIWs inside the eddy gradually moved towards the center of the eddy and reached 800 m 12 days after the typhoon's passage. The anticyclonic

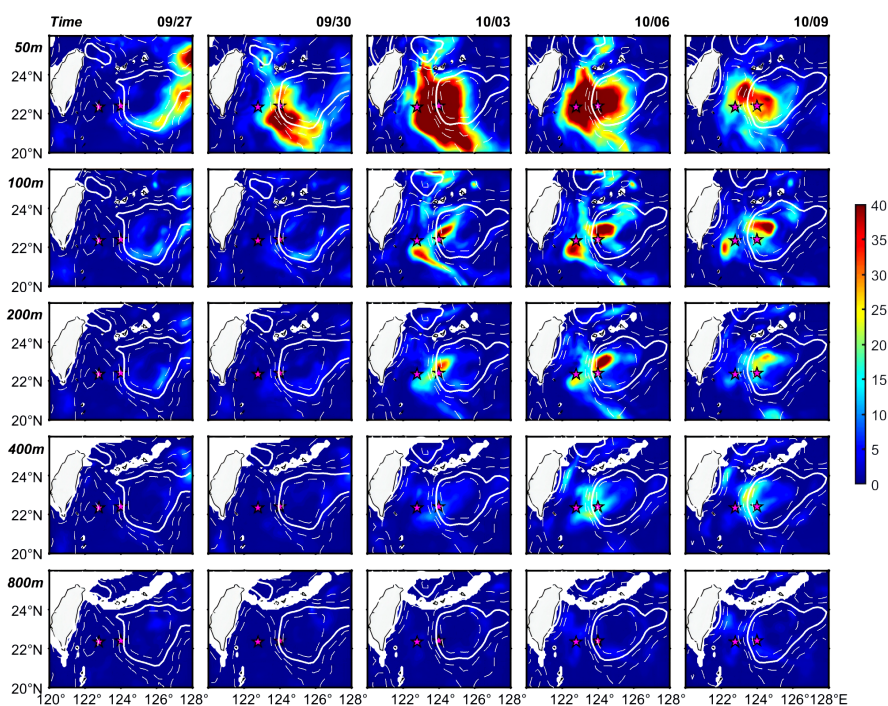


FIGURE 5

Time evolution of NIKE (unit: J/m^3) generated by Typhoon MITAG at different depths from 27 September to 9 October. Superimposed white line is the SLA contours with an interval of 0.06 m, and thick white line indicates the 0.18 m contour. Pink stars represent the locations of moorings. The number at the top represents the time of each column, and the depth of each row is marked in bold italics on the far left.

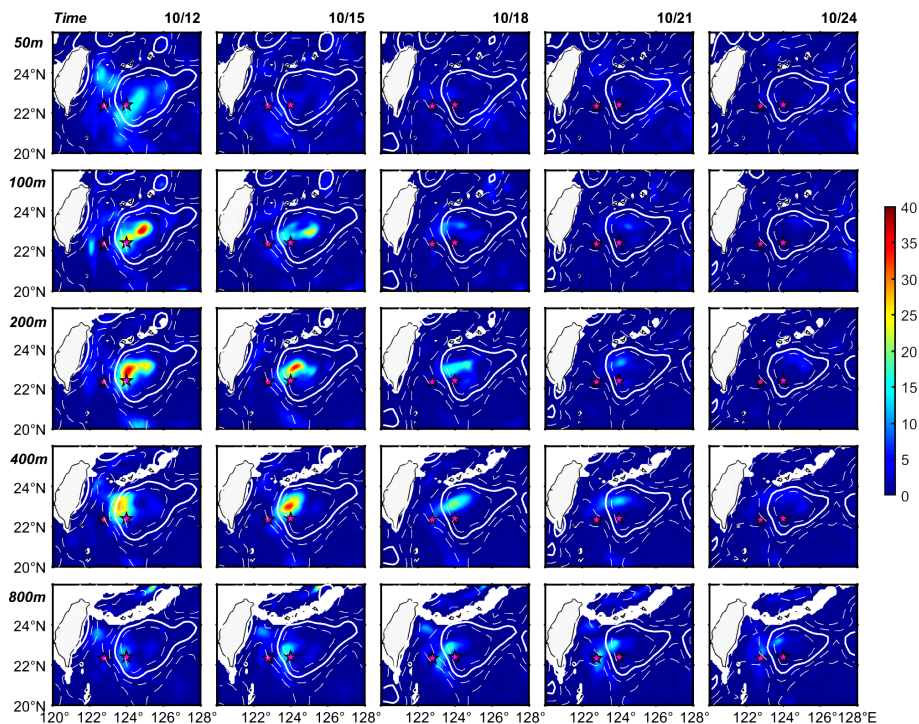


FIGURE 6
Time evolution of NIKE (unit: J/m^3) generated by Typhoon MITAG at different depths from 12 to 24 October. All other elements are the same as in Figure 5.

eddy significantly prolonged the duration of NIWs and facilitated the propagation of NIWs to the deep sea. This was also the main reason for the large disparity between the observations of the two moorings.

In addition, the near-inertial energy flux (Figure 4) showed strong energy input to the Kuroshio east of Taiwan, but there was no significant enhancement of NIKE under 50 m west of 122.5°E. According to Jeon (Jeon et al., 2019), after the typhoon’s passage, strong NIKE existed upstream of the Kuroshio east of Taiwan at 4 m, but at 100 m, NIKE began to appear only north of 25°N. Therefore, this phenomenon may be due to advection of the

upstream Kuroshio, with NIWs being carried poleward before propagating downwards.

4.3 E-folding time

Figure 7 illustrates the e-folding time of depth-integrated NIKE to better understand the damping of MITAG-generated NIWs. Except for the Kuroshio on the northeast side of Taiwan, the e-folding scale along MITAG’s path was below 5 days. High e-folding time areas were located inside the anticyclonic eddy and along its

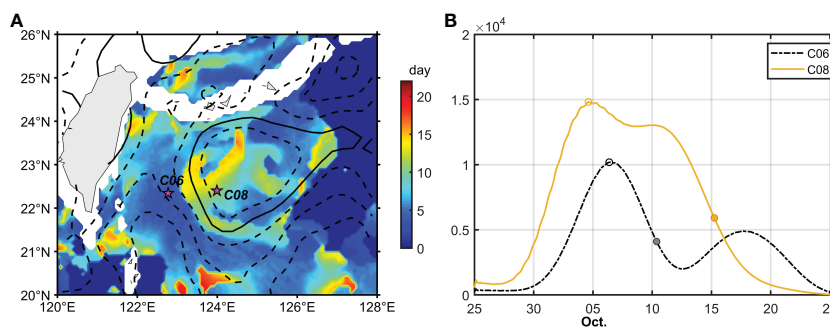


FIGURE 7
Distribution of e-folding time of depth-integrated NIKE east of Taiwan (A). Superimposed black line is the time-averaged (from 30 September to 24 October) SLA contours with an interval as Figure 5. Pink stars represent the locations of moorings. Time evolution of depth-integrated NIKE at different points (B) (unit: J/m^2). The filled and empty circles represent the maximum and e-folding values of depth-integrated NIKE.

southwestern edge. The latter was largely distributed along the SLA contours and ranged from 2 to 3 weeks. With reference to the spatial distribution of NIKE (Figures 5, 6), it is clear that the high values south of 21°N may be due to the persistence of weak near-inertial energy (less than $0.2 \times 10^{-8} \text{ J/m}^2$).

Moorings C06 and C08 can represent different situations in and outside the eddy, and their time series are shown in Figure 7B. To the right side of MITAG’s path, the NIKE peaked more quickly and gained more energy at C08, leading to an earlier start of e-folding time. At the same time, the dissipation at C08 was slower with a smaller rate of the time series in the eddy, and there was a small increase in energy from 8 October, which then started to decay again, leading to a later end of the e-folding time. As a result, the e-folding scales at the two moorings differed significantly, with time at C06 outside the eddy less than 1 week and time at C08 in the eddy more than 2 weeks. The time series at C06 first decayed close to zero and then reached a second peak on approximately 18 October, which corresponds to the deeper weaker NIKE in Figure 2B. The reasons for this phenomenon are explored in detail in Section 5.2.

4.4 Energy flux

To investigate the characteristics of the vertical propagation of this near-inertial event, the near-inertial vertical energy flux (F_E) was calculated for the main area where MITAG generated NIKE. The calculation of F_E can be obtained by (Nash et al., 2005):

$$F_E = C_{gz}E \tag{10}$$

where C_{gz} is the vertical group velocity and E is the near-inertial energy. To simplify the calculation, the mean value of C_{gz} of moorings C06 and C08 was substituted into Equation (10). C_{gz}

can be estimated by identifying the downwards progression of kinetic energy maxima over time (Yu et al., 2022), resulting in 7.53 m/d at C06 and 38.82 m/d at C08. The time-averaged (from 30 September to 24 October) SLA was used to determine the edge of the eddy (Figure 8 black solid line) and then the F_E outside and in the eddy was calculated, as shown in Figures 8A, B. The F_E in the eddy is an order of magnitude higher than that outside the eddy. Before October 10, the F_E in and outside the eddy both gradually extended deeper, but the speed was faster in the eddy. The F_E outside the eddy was on the order of 10^{-4} under 500 m, which was essentially negligible. The downwards transmission of these NIWs was very weak, probably due to the viscous effect of seawater, and less efficient than that occurring in the anticyclonic eddy. After 10 October, the F_E outside the eddy had completely decayed, while the F_E in the eddy formed two high value areas bounded by 300 m.

As shown in Figure 8C, the mean near-inertial F_E generated by Typhoon MITAG decayed rapidly in the mixed layer, and the rate of damping decreased below the thermocline. Thirty-five percent of the energy crossed the thermocline, but at 800 m, only 12.8% of the F_E remains. The time-averaged F_E in the anticyclonic eddy after 10 October is shown in Figure 8D. There were two significant peaks in the changing curve of F_E , with the shallower one at 140 m. This corresponds to the peak in time-averaged buoyancy frequency (N^2) at approximately 140 m (Figure 8E). The amplitude, energy and vertical wavenumber of NIWs were constantly adjusted due to the refraction of different stratifications. Therefore, the effect of N^2 on NIWs may be largely responsible for the shallow peak of F_E . Theory, models and observations all suggest that NIWs encounter a critical layer in the vertical direction when captured by anticyclonic eddies (Kunze, 1985; Lee and Niiler, 1998; Zhai et al., 2005; Lelong et al., 2020). The F_E curve weakens from the first peak to 300 m and then begins to strengthen again, reaching the second peak at 500 m. This reveals that the critical layer is approximately 500 m and that the F_E

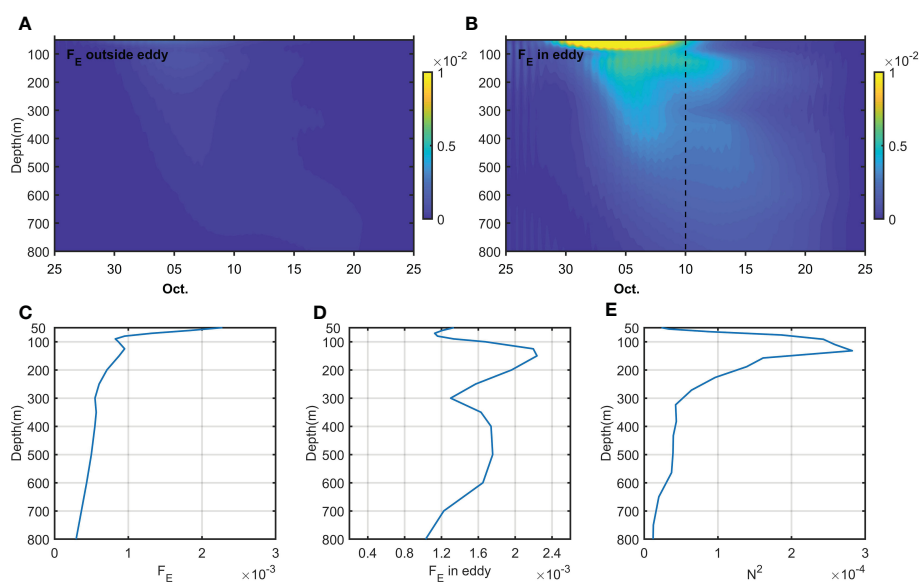


FIGURE 8 Time evolution of F_E outside (A) and in (B) the eddy (unit: W/m^2). The black dashed line indicates the time when F_E in eddy starts to form two peaks in D (10 October). Variation of F_E in the region east of Taiwan (C), F_E in the eddy from 10 to 25 October (D) and Buoyancy frequency (E) with depth.

near the critical layer is significantly higher than the regional averaged results in Figure 8C.

For results averaged over the main area, most of the NIKE remains above the thermocline, and the anticyclonic eddy does not observably increase the proportion of NIKE propagating from the thermocline to the deeper layers. Nevertheless, NIKE propagating through the thermocline is found to occur predominantly in the anticyclonic eddy, leading to enhancement of F_E from 400 to 600 m. The transfer of NIWs from outside the eddy to the deep layer is minimal. Therefore, anticyclonic eddies play a crucial role in the transfer of more near-inertial energy to the deep ocean.

4.5 Release of near-inertial energy

Theoretical analysis and numerical models indicate that the mean flow absorbs most of the wave energy in the critical layer (Thorpe, 1981; Altman, 1988). To investigate the process of energy release in the anticyclonic eddy, we calculated the background flow kinetic energy (KE) outside and in the eddy (Figure 9). Before the passage of typhoon MITAG, the KE in the eddy was significantly lower than that outside the eddy, but they both showed a tendency to decrease. The decay rate of KE outside the eddy decreased after the typhoon's passage, and KE remained largely unchanged from October 5. While KE in the eddy was converted from decay to increase, the background flow KE was enhanced from 50 m to 800 m. It does not take long for the KE in the anticyclonic eddy to exceed that before the arrival of MITAG, and it was even higher than the KE outside the eddy after 10 October. The biggest difference in these two regions, in and outside the eddy, after the passage of MITAG is the near-inertial energy flux. Combined with the results in Section 4.4, it can be illustrated that the downwards propagation of NIWs leads to the enhancement of the background flow KE. Osborn states that although 80% of the internal wave energy will be dissipated by turbulence, some of them will modulate the background flow (Osborn, 1980). Because of the low vertical resolution of the HYCOM data, we were unable to explore in detail the turbulent dissipation and could not obtain the proportion of energy transferred from NIWs to the background flow. However, this result is sufficient to confirm the existence of an inverse energy cascade between NIWs and background flow energy in the anticyclonic eddy, which has important implications for the study of the energy source of deep-sea mixing. At present, various models

simulate results for deep sea circulation that are smaller than those actually observed. The propagation of NIWs to the deep sea and the increase in background flow kinetic energy in anticyclonic eddies are worthy of attention.

5 Discussion

5.1 Mode structure

Decompose the near-inertial currents of HYCOM into vertical modes from 0 to 800 m, and perform a depth integration for different modes (Figures 10, 11). Examples of applying this method to the range from the surface to the maximum depth that NIWs can reach were common in previous work (Chen et al., 2013; Hou et al., 2019; Huang et al., 2021), so the range of 0-800 m selected for this study is fairly reasonable.

Calculations show that the initial widespread distribution of NIKE generated by MITAG was dominated by the first two modes. They fully dissipated after 12 October and existed for two weeks. The energy of the third mode mainly gathered to the south of mooring C06 until 12 October, and as the first two modes dissipated, the third mode formed more energy near mooring C08. Both the third mode and the sum of the higher modes (modes from 4 to 20, $\Sigma 4-20$) split into two parts inside and outside the eddy. The energy south of C06 rapidly dissipated, while the energy inside the eddy was gradually enhanced. Eventually, the energy of $\Sigma 4-20$ disappeared completely on 24 October. The mode structure indicates that the energy captured by the anticyclonic eddy is composed mainly of higher modes. In the absence of the anticyclonic eddy, referring to NIWs near C06, energy is rapidly transferred to the third mode and $\Sigma 4-20$ and is completely dissipated in the case that the third mode contains the most energy. However, under the influence of the eddy, the energy of the higher modes continues to increase and exceeds that of the first three modes. This phenomenon can be maintained for more than one week.

The vertical distribution of energy for each mode was also explored (Figures S3-S6). NIKE of the third mode is stronger at 50 m, 200 m and 800 m and is concentrated on the western edge of the mesoscale eddy. The NIKE of $\Sigma 4-20$ started to appear at 800 m on 3 October and then gradually intensified. Therefore, NIKE at 800 m consists mainly of the third mode and $\Sigma 4-20$. Compared to mode 3

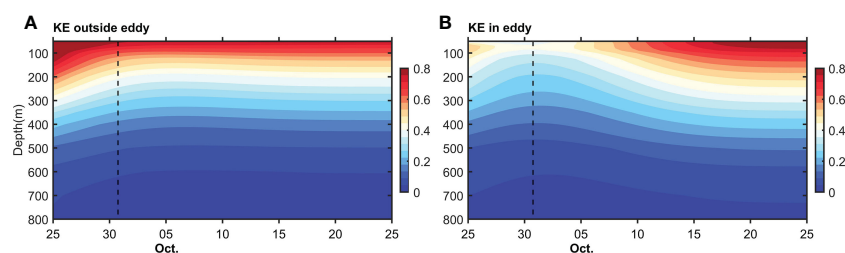


FIGURE 9

KE of background flow outside (A) and in (B) the eddy (unit: J/m^3). The black dashed lines represent the time when MITAG left the sea area east of Taiwan (18:00 30 September).

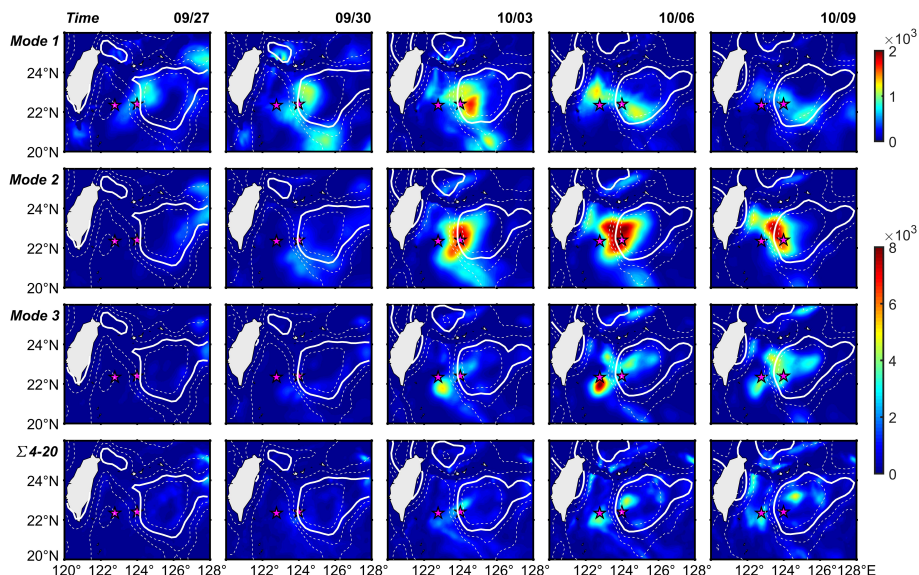


FIGURE 10
Time evolution of depth-integrated NIKE (unit: J/m^2) of different modes from 27 September to 9 October. Mode name is marked in black italic on the leftmost side. Other elements are the same as Figure 5. Note that mode1 has a different colorbar to the other modes.

at 800 m, the core of $\Sigma 4-20$ is closer to the center of the eddy and is composed of NIWs captured by the eddy (Buhler and McIntyre, 2005). Several previous investigations have recognized that the evolution of a eddy consists of three different stages. In the second stage, the eddy loses energy through the excitation of internal waves (Liao et al., 2019). Thus the high value of the third mode at 800 m may be related to the energy dissipation of the mesoscale eddies during their evolution.

5.2 Propagation along the zonal section of moorings

The NIKE from both mooring and HYCOM data at C06 consists of two parts: one is directly generated by typhoon MITAG and dissipates above 400 m, and the other below 400 m only starts to strengthen after 12 October. To find the source of the second part, Figure 12A illustrates the depth-integrated NIKE along

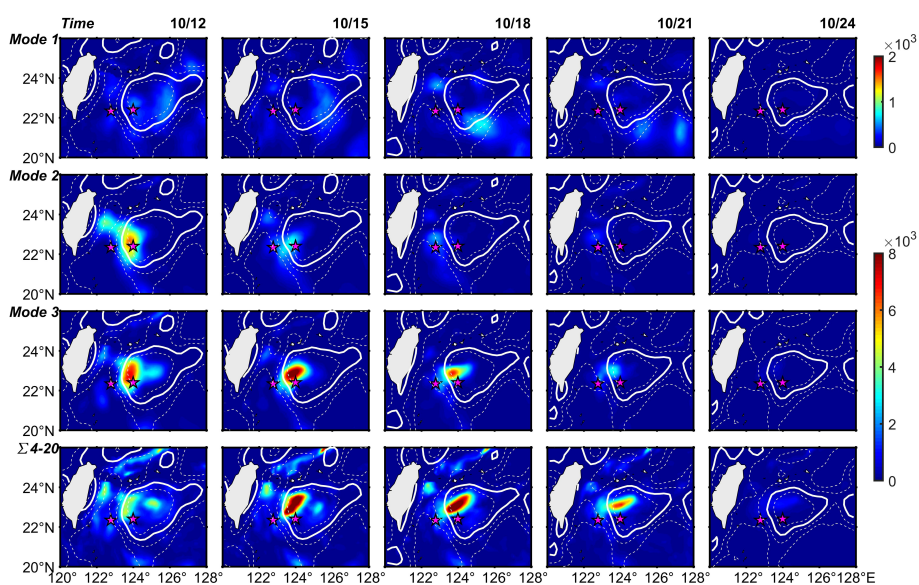


FIGURE 11
Time evolution of depth-integrated NIKE (unit: J/m^2) of different modes from 12 to 24 October. All other elements are the same as Figure 5.

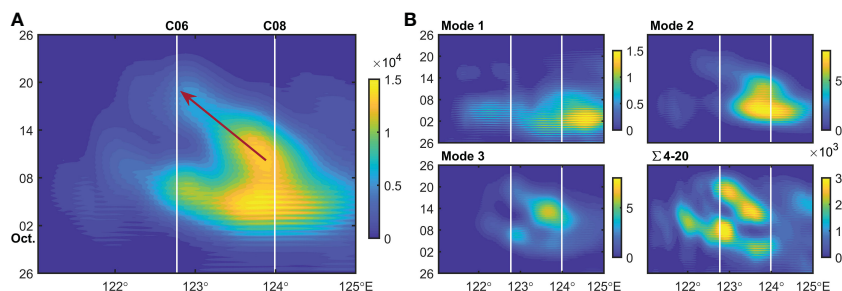


FIGURE 12

Variation of depth-integrated NIKE (unit: J/m^2) of total (A) and different modes (B) along 22.4°N . The horizontal axis represents longitude and the vertical axis represents time. The white vertical lines show the longitude of moorings C06 and C08.

the zonal section of moorings (22.4°N). The NIKE east of 123.5°E is coherent over time and appeared before the energy at C06. This is because typhoon MITAG initially formed east of 123.5°E , and this region was always located to the right side of the typhoon center. This part of the NIKE showed a tendency to propagate westwards from 10 October. The typhoon-generated NIKE at C06 was weaker and decayed on approximately 10 October. Subsequently, the westwards propagating NIKE east of 123.5°E reached and formed the second part of the NIKE at C06.

The results of the dynamic mode decomposition (Figure 12B) indicate that the first part of the energy at C06 from October 6 to October 10 was dominated by $\Sigma 4-20$. At C08, NIKE before 10 October consisted mainly of the first two modes, then mode 3 and $\Sigma 4-20$ gradually account for the major contribution. The main component of the westwards propagating energy is $\Sigma 4-20$, revealed a westwards transfer of mixing and dissipation. It is estimated that the duration of propagation along 22.4°N was from 10 October to 20 October, with a distance of approximately 92.63 km. Therefore, the zonal energy movement speed on average is $u_{\text{NIW}} = -0.107 \text{ m/s}$ (negative sign represents westwards flow). The zonal component of depth-averaged background flow at the eddy's edge is $u = -0.104 \text{ m/s}$, almost the same speed as u_{NIW} . Thus, the energy source for the second part at C06 was the typhoon-generated NIKE east of 123.5°E , which advected westwards by the background flow.

6 Conclusions

Based on the observations of two moorings and HYCOM data, the generation and propagation of NIWs caused by Typhoon MITAG east of Taiwan was investigated in detail. As HYCOM data were able to simulate this near-inertial event well, HYCOM data was mainly used to reveal the influence of an anticyclonic eddy on NIWs. We conclude that the reason for the difference between the two moorings is that C08 is influenced by an anticyclonic eddy. The effect of the eddy is to increase the near-inertial energy flux and facilitate the propagation of NIWs to the deep ocean. We also confirm that there is a transfer of near-inertial energy to the background flow energy in the anticyclonic eddy.

By observing HYCOM data layer by layer, it was found that Typhoon MITAG rapidly generated strong NIKE in the upper ocean along its path and input a large amount of energy into the sea area east of Taiwan. Most NIKE propagated towards the negative vorticity. The NIKE outside the anticyclonic eddy could not cross the thermocline and dissipated within a week. The energy near the edge gradually moved towards the eddy center and reached 800 m 12 days after the typhoon's passage. High value areas of e-folding time were located inside the anticyclonic eddy and its southwestern edge, and the time was longer when it is closer to the eddy center.

For results averaged over the main area, 75% of the NIKE was confined above the thermocline. Although no significant influence of the anticyclonic eddy could be seen in the averaged F_E , the NIKE propagating through the thermocline into the deep ocean was mainly concentrated within the eddy. There was a clear enhancement of F_E near the critical layer from 400 to 600 m. After the passage of MITAG, the transfer of NIWs from outside the eddy to the deep ocean was minimal and did not affect the background flow. In contrast, the downward propagation of NIWs in the anticyclonic eddy enhanced the background flow kinetic energy.

In the absence of anticyclonic eddies, NIKE was dominated by the second mode at the beginning, and then the third mode accounted for the major contribution. NIKE in the eddy was characterized by the dominance of the fourth and higher modes. Moreover, the time when the proportion of higher modes started to increase coincided with the time when depth-averaged NIKE began to enhance, suggesting that the anticyclonic eddy primarily captured higher mode NIWs. In the eddy, the state of continuous energy growth of higher modes could be maintained for more than a week. In addition, the advection effect of the background flow was investigated. The mean background flow at the edge of the mesoscale eddy carried NIWs westwards. Although the flow was weak, it still enabled NIKE to move 92.63 km in 10 days.

In summary, anticyclonic eddies play a crucial role in the horizontal and vertical propagation of NIWs. It can cause NIKE from the eddy edge to accumulate towards the eddy center and enable the propagation of NIWs to the deep sea. Meanwhile, anticyclonic eddies also influence the damping of NIWs, which promotes the enhancement of near-inertial energy flux near the

critical layer and significantly extends the duration of NIWs. Furthermore, the anticyclonic eddy captures mainly NIWs of high modes, and there is a continuous increase in the energy of high modes in the eddy. The existence of an inverse energy cascade between NIKE and background flow kinetic energy in the anticyclonic eddy was also confirmed. Thus, our research related to the influence of anticyclonic eddies on NIWs has important significance for understanding ocean mixing and energy dissipation and can provide new ideas for improving the modelling of deep sea circulation.

Data availability statement

The original contributions presented in the study are included in the article/Supplementary Material. Further inquiries can be directed to the corresponding author.

Author contributions

TZ designed the experiment, conducted the analyses, and wrote the manuscript. FY and FN contributed to the designed test, supervised the manuscript, and provided revisions. QR, ZC, YH, and Y-ND participated in the observation data collection and formal analysis. ZC and YL participated in the discussions and improvement of the manuscript. All authors contributed to the article and approved the submitted version.

References

- Alford, M. H. (2001). Internal swell generation: The spatial distribution of energy flux from the wind to mixed layer near-inertial motions. *J. Phys. Oceanogr.* 31, 2359–2368. doi: 10.1175/1520-0485(2001)031<2359:ISGTS>2.0.CO;2
- Alford, M. H. (2003). Redistribution of energy available for ocean mixing by long-range propagation of internal waves. *Nature* 423, 159–162. doi: 10.1038/nature01628
- Alford, M. H. (2020). Global calculations of local and remote near-Inertial-Wave dissipation. *J. Phys. Oceanogr.* 50, 3157–3164. doi: 10.1175/JPO-D-20-0106.1
- Alford, M. H., Cronin, M. F., and Klymak, J. M. (2012). Annual cycle and depth penetration of wind-generated near-inertial internal waves at ocean station papa in the northeast pacific. *J. Phys. Oceanogr.* 42, 889–909. doi: 10.1175/JPO-D-11-092.1
- Alford, M. H., MacKinnon, J. A., Simmons, H. L., and Nash, J. D. (2016). Near-inertial internal gravity waves in the ocean. *Annu. Rev. Mar. Sci.* 8, 95–123. doi: 10.1146/annurev-marine-010814-015746
- Alford, M. H., and Whitmont, M. (2007). Seasonal and spatial variability of near-inertial kinetic energy from historical moored velocity records. *J. Phys. Oceanogr.* 37, 2022–2037. doi: 10.1175/JPO3106.1
- Altman, D. B. (1988). Critical layers in accelerating 2-layer flows. *J. Fluid Mech.* 197, 429–451. doi: 10.1017/S0022112088003313
- Buhler, O., and McIntyre, E. (2005). Wave capture and wave-vortex duality. *J. Fluid Mech.* 534, 67–95. doi: 10.1017/S0022112005004374
- Cao, A. Z., Guo, Z., Pan, Y. H., Song, J. B., He, H. L., and Li, P. L. (2021). Near-inertial waves induced by typhoon megii (2010) in the south China Sea. *J. Mar. Sci. Eng.* 9, 440. doi: 10.3390/jmse9040440
- Chelton, D. B., Schlax, M. G., and Samelson, R. M. (2011). Global observations of nonlinear mesoscale eddies. *Prog. Oceanogr.* 91, 167–216. doi: 10.1016/j.pcean.2011.01.002
- Chen, S. L., Hu, J. Y., and Polton, J. A. (2015). Features of near-inertial motions observed on the northern south China Sea shelf during the passage of two typhoons. *Acta Oceanol. Sin.* 34, 38–43. doi: 10.1007/s13131-015-0594-y
- Chen, G., Xue, H., Wang, D., and Xie, Q. (2013). Observed near-inertial kinetic energy in the northwestern south China Sea. *J. Geophys. Res. Oceans* 118, 4965–4977. doi: 10.1002/jgrc.20371
- D'Asaro, E. A., Eriksen, C. C., Levine, M. D., Niiler, P., Paulson, C. A., and Meurs, P. V. (1995). Upper-ocean inertial currents forced by a strong storm. part I: Data and comparisons with linear theory. *J. Phys. Oceanogr.* 25, 2909–2936. doi: 10.1175/1520-0485(1995)025<2909:UOICFB>2.0.CO;2
- Elipot, S., Lumpkin, R., and Prieto, G. (2010). Modification of inertial oscillations by the mesoscale eddy field. *J. Geophys. Res. Ocean.* 115, C09010. doi: 10.1029/2009JC005679
- Flexas, M. M., Thompson, A. F., Torres, H. S., Klein, P., Farrar, J. T., Zhang, H., et al. (2019). Global estimates of the energy transfer from the wind to the ocean, with emphasis on near-inertial oscillations. *J. Geophys. Res. Oceans* 124, 5723–5746. doi: 10.1029/2018JC014453
- Furuichi, N., Hibiya, T., and Niwa, Y. (2008). Model-predicted distribution of wind-induced internal wave energy in the world's oceans. *J. Geophys. Res.* 113, C09034. doi: 10.1029/2008JC004768
- Gill, A. E. (1982). *Atmosphere–ocean dynamics* (Academic Press), 662.
- Gill, A. E. (1984). On the behavior of internal waves in the wake of a storm. *J. Phys. Oceanogr.* 14, 1129–1151. doi: 10.1175/1520-0485(1984)014<1129:OTBOIW>2.0.CO;2
- Greatbatch, R. J. (1984). On the response of the ocean to a moving storm: Parameters and scales. *J. Phys. Oceanogr.* 14, 59–78. doi: 10.1175/1520-0485(1984)014<0059:OTROTO>2.0.CO;2
- Hisaki, Y., and Naruke, T. (2003). Horizontal variability of near-inertial oscillations associated with the passage of a typhoon. *J. Geophys. Res. Oceans* 108, 3382. doi: 10.1029/2002JC001683
- Hou, H., Yu, F., Nan, F., Yang, B., Guan, S., and Zhang, Y. (2019). Observation of near-inertial oscillations induced by energy transformation during typhoons. *Energies* 12, 99. doi: 10.3390/en12010099

Funding

This work was supported by the Shandong province Natural Science Fund (Grant No. ZR2022QD045 and ZR2020MD057), National Natural Science Foundation of China (Grant No.42206032 and 42106196), and National Key R&D Program of China (Grant No.2022YFC3104100).

Conflict of interest

The authors declare that the research was conducted in the absence of any commercial or financial relationships that could be construed as a potential conflict of interest.

Publisher's note

All claims expressed in this article are solely those of the authors and do not necessarily represent those of their affiliated organizations, or those of the publisher, the editors and the reviewers. Any product that may be evaluated in this article, or claim that may be made by its manufacturer, is not guaranteed or endorsed by the publisher.

Supplementary material

The Supplementary Material for this article can be found online at: <https://www.frontiersin.org/articles/10.3389/fmars.2023.1117197/full#supplementary-material>

- Hu, S., Liu, L., Guan, C., Zhang, L., and Hu, D. (2020). Dynamic features of near-inertial oscillations in the Northwest Pacific derived from mooring observations from 2015 to 2018. *J. Oceanol. Limnol.* 38, 1092–1107. doi: 10.1007/s00343-020-9332-1
- Hu, D. X., Wu, L. X., Cai, W. J., Sen Gupta, A., Ganachaud, A., Qui, B., et al. (2015). Pacific western boundary currents and their roles in climate. *Nature* 522, 299–308. doi: 10.1038/nature14504
- Huang, R., Xie, X., Hu, J., and Sun, Z. (2021). Poleward propagation of typhoon-induced near-inertial waves in the northern south China Sea. *Front. Mar. Sci.* 8. doi: 10.3389/fmars.2021.713991
- Jaimes, B., and Shay, L. K. (2010). Near-inertial wave wake of hurricanes Katrina and Rita over mesoscale oceanic eddies. *J. Phys. Oceanogr.* 40, 1320–1337. doi: 10.1175/2010JPO4309.1
- Jeon, C., Park, J. H., Nakamura, H., Nishina, A., Zhu, X. H., Kim, D. G., et al. (2019). Poleward-propagating near-inertial waves enabled by the western boundary current. *Sci. Rep.* 9, 9955. doi: 10.1038/s41598-019-46364-9
- Jiang, J., Lu, Y., and Perrie, W. (2005). Estimating the energy flux from the wind to ocean inertial motions: The sensitivity to surface wind fields. *Geophys. Res. Lett.* 32, 291–310. doi: 10.1029/2005GL023289
- Jochum, M., Briegleb, B. P., Danabasoglu, G., Large, W. G., Norton, N. J., Jayne, S. R., et al. (2013). The impact of oceanic near-inertial waves on climate. *J. Clim.* 26, 2833–2844. doi: 10.1175/JCLI-D-12-00181.1
- Johnston, T. M. S., Wang, S. G., Lee, C. Y., Moum, J. N., Rudnick, D. L., and Sobel, A. (2021). Near-inertial wave propagation in the wake of super typhoon mangkhut: Measurements from a profiling float array. *J. Geophys. Res. Oceans* 126, e2020JCO16749. doi: 10.1029/2020JCO16749
- Kim, E., Jeon, D., Jang, C. J., and Park, J. H. (2013). Typhoon rammasun-induced near-inertial oscillations observed in the tropical northwestern Pacific ocean. *Terr. Atmos. Ocean. Sci.* 24, 761–772. doi: 10.3319/TAO.2013.03.28.01(Oc)
- Kunze, E. (1985). Near-inertial wave propagation in geostrophic shear. *J. Phys. Oceanogr.* 15, 544–565. doi: 10.1175/1520-0485(1985)015<0544:NIWPIG>2.0.CO;2
- Lee, D. K., and Niiler, P. P. (1998). The inertial chimney: The near-inertial energy drainage from the ocean surface to the deep layer. *J. Geophys. Res. Oceans* 103, 7579–7591. doi: 10.1029/97JC03200
- Lelong, M. P., Cuypers, Y., and Bouruet-Aubertot, P. (2020). Near-inertial energy propagation inside a Mediterranean anticyclonic eddy. *J. Phys. Oceanogr.* 50, 2271–2288. doi: 10.1175/JPO-D-19-0211.1
- Liao, G. H., Xu, X. H., Dong, C. M., Cao, H. J., and Wang, T. (2019). Three-dimensional baroclinic eddies in the ocean: Evolution, propagation, overall structures, and angular models. *J. Phys. Oceanogr.* 49, 2571–2599. doi: 10.1175/JPO-D-18-0237.1
- Lin, X. Y., Dong, C. M., Chen, D. K., Liu, Y., Yang, J. S., Zou, B., et al. (2015). Three-dimensional properties of mesoscale eddies in the south China Sea based on eddy-resolving model output. *Deep-Sea Res. Part I-Oceanogr. Res. Pap.* 99, 46–64. doi: 10.1016/j.dsr.2015.01.007
- Liu, Y. Z., Jing, Z., and Wu, L. X. (2019). Wind power on oceanic near-inertial oscillations in the global ocean estimated from surface drifters. *Geophys. Res. Lett.* 46, 2647–2653. doi: 10.1029/2018GL081712
- Nash, J. D., Alford, M. H., and Kunze, E. (2005). Estimating internal wave energy fluxes in the ocean. *J. Atmos. Ocean. Technol.* 22, 1551–1570. doi: 10.1175/JTECH1784.1
- Nikurashin, M., and Legg, S. (2011). A mechanism for local dissipation of internal tides generated at rough topography. *J. Phys. Oceanogr.* 41, 378–395. doi: 10.1175/2010JPO4522.1
- Osborn, T. R. (1980). Estimates of the local rate of vertical diffusion from dissipation measurements. *J. Phys. Oceanogr.* 10, 83–89. doi: 10.1175/1520-0485(1980)010<0083:EOTLRO>2.0.CO;2
- Pallas-Sanz, E., Candela, J., Sheinbaum, J., Ochoa, J., and Jouanno, J. (2016). Trapping of the near-inertial wave wakes of two consecutive hurricanes in the loop current. *J. Geophys. Res. Oceans* 121, 7431–7454. doi: 10.1002/2015JC011592
- Park, J. H., and Watts, D. R. (2005). Near-inertial oscillations interacting with mesoscale circulation in the southwestern Japan/East Sea. *Geophys. Res. Lett.* 32, L10611. doi: 10.1029/2005GL022936
- Pollard, R. T., and Millard, R. C. (1970). Comparison between observed and simulated wind-generated inertial oscillations. *Deep-Sea Res. Oceanogr. Abstr.* 17, 153–175. doi: 10.1016/0011-7471(70)90043-4
- Price, J. F., Weller, R. A., and Pinkel, R. (1986). Diurnal cycling: Observations and models of the upper ocean response to diurnal heating, cooling, and wind mixing. *J. Geophys. Res.* 97, 8411–8427. doi: 10.1029/JC091iC07p08411
- Rainville, L., and Pinkel, R. (2004). Observations of energetic high-wavenumber internal waves in the kuroshio. *J. Phys. Oceanogr.* 34, 1495–1505. doi: 10.1175/1520-0485(2004)034<1495:OOEHIW>2.0.CO;2
- Raja, K. J., Buijsman, M. C., Shriver, J. F., Arbic, B. K., and Siyanbola, O. (2022). Near-inertial wave energetics modulated by background flows in a global model simulation. *J. Phys. Oceanogr.* 52, 823–840. doi: 10.1175/JPO-D-21-0130.1
- Shay, L. K., Elsberry, R. L., and Black, P. G. (1989). Vertical structure of the ocean current response to a hurricane. *J. Phys. Oceanogr.* 19, 649–669. doi: 10.1175/1520-0485(1989)019<0649:VSOTOC>2.0.CO;2
- Silverthorne, K. E., and Toole, J. M. (2009). Seasonal kinetic energy variability of near-inertial motions. *J. Phys. Oceanogr.* 39, 1035–1049. doi: 10.1175/2008JPO3920.1
- Simmons, H. L., and Alford, M. H. (2012). Simulating the long-range swell of internal waves generated by ocean storms. *Oceanography* 25, 30–41. doi: 10.5670/oceanog.2012.39
- Sun, Z., Hu, J., Zheng, Q., and Li, C. (2011). Strong near-inertial oscillations in geostrophic shear in the northern south China Sea. *J. Oceanogr.* 67, 377–384. doi: 10.1007/s10872-011-0038-z
- Sun, L., Zheng, Q., Wang, D., Hu, J., Tai, C. K., and Sun, Z. (2011). A case study of near-inertial oscillation in the south China Sea using mooring observations and satellite altimeter data. *J. Oceanogr.* 67, 677–687. doi: 10.1007/s10872-011-0081-9
- Thorpe, S. E. (1981). An experimental study of critical layers. *J. Fluid Mech.* 103, 321–344. doi: 10.1017/S0022112081001365
- Thorpe, S. A., and Jiang, R. (1998). Estimating internal waves and diapycnal mixing from conventional mooring data in a lake. *Limnol. Oceanogr.* 43, 936–945. doi: 10.4319/lo.1998.43.5.0936
- Webster, F. (1968). Observations of inertial-period motions in the deep sea. *Rev. Geophys.* 6, 473. doi: 10.1029/RG006i004p00473
- Weller, R. A. (1982). The relation of near-inertial motions observed in the mixed layer during the JASIN (1978) experiment to the local wind stress and to the quasi-geostrophic flow field. *J. Phys. Oceanogr.* 12, 1122–1136. doi: 10.1175/1520-0485(1982)012<1122:TRONIM>2.0.CO;2
- Whalen, C. B., MacKinnon, J. A., and Talley, L. D. (2018). Large-Scale impacts of the mesoscale environment on mixing from wind-driven internal waves. *Nat. Geosci.* 11, 842–847. doi: 10.1038/s41561-018-0213-6
- Yang, B., Hou, Y., Hu, P., Liu, Z., and Liu, Y. (2015). Shallow ocean response to tropical cyclones observed on the continental shelf of the northwestern south China Sea. *J. Geophys. Res. Ocean.* 120, 3817–3836. doi: 10.1002/2015JC010783
- Yang, B., Hu, P., and Hou, Y. (2021). Observed near-inertial waves in the northern south China Sea. *Remote Sens.* 13, 3223. doi: 10.3390/rs13163223
- Yu, X. L., Garabato, A. C. N., Vic, C., Gula, J., Savage, A. C., Wang, J. B., et al. (2022). Observed equatorward propagation and chimney effect of near-inertial waves in the midlatitude ocean. *Geophys. Res. Lett.* 49, e2022GL098522. doi: 10.1029/2022GL098522
- Zhai, X. M., Greatbatch, R. J., and Zhao, J. (2005). Enhanced vertical propagation of storm-induced near-inertial energy in an eddying ocean channel model. *Geophys. Res. Lett.* 32, L18602. doi: 10.1029/2005GL023643
- Zhang, Z., Qiu, B., Tian, J., Zhao, W., and Huang, X. (2018). Latitude-dependent finescale turbulent shear generations in the Pacific tropic-extratropical upper ocean. *Nat. Commun.* 9, 4086. doi: 10.1038/s41467-018-06260-8